


Feature Review

Iron, Myelin, and the Brain: Neuroimaging Meets Neurobiology

Harald E. Möller ^{1,*} Lucia Bossoni,² James R. Connor,³ Robert R. Crichton,⁴ Mark D. Does,⁵ Roberta J. Ward,⁶ Luigi Zecca,^{7,8} Fabio A. Zucca,⁷ and Itamar Ronen²

Although iron is crucial for neuronal functioning, many aspects of cerebral iron biology await clarification. The ability to quantify specific iron forms in the living brain would open new avenues for diagnosis, therapeutic monitoring, and understanding pathogenesis of diseases. A modality that allows assessment of brain tissue composition *in vivo*, in particular of iron deposits or myelin content on a submillimeter spatial scale, is magnetic resonance imaging (MRI). Multimodal strategies combining MRI with complementary analytical techniques *ex vivo* have emerged, which may lead to improved specificity. Interdisciplinary collaborations will be key to advance beyond simple correlative analyses in the biological interpretation of MRI data and to gain deeper insights into key factors leading to iron accumulation and/or redistribution associated with neurodegeneration.

Toward *In Vivo* Histochemistry?

Our understanding of the broad principles of human cellular iron biology and cellular and systemic iron homeostasis is well established, with the exception of the brain [1]. In recent years, brain iron accumulation has gained substantial research interest in the context of aging and neurodegeneration. This is not least due to empirical evidence obtained using magnetic resonance imaging (MRI). Iron is a major contributor to the **relaxation** (see [Glossary](#)) and **magnetic susceptibility** of brain tissue [2–5]. Ironically, the presence of compounds of different susceptibility, being a source of artifacts, have long been considered a nuisance for MRI rather than a benefit. Meanwhile, it is recognized that susceptibility-sensitive MRI offers unique possibilities to estimate iron content *in vivo*. Further differentiation of particular molecular forms of iron will be an essential step towards understanding functional pathways or mechanisms underlying iron accumulation. However, the MRI signal is not only affected by the presence of iron compounds. Strong contrast between white matter (WM) and gray matter (GM) hints at important contributions of myelin to relaxation [6] and magnetic susceptibility [7,8]. A joint consideration of both entities is also motivated from a biological perspective because iron is required for myelin formation and maintenance [9].

Consequently, there is a timely need for collaborations between imaging physicists and iron biologists. Integration of complementary analytical techniques ([Box 1](#)) is necessary to understand contributions to the MRI signal and provide gold standards for validation. For synergy between advances in methodology and cell biology, it is important to bridge conceptual gaps between traditionally separated disciplines. To reinforce this, we first introduce how brain tissue is characterized using MRI. We then integrate ‘what can be measured’ into a context of myelin neurobiology and iron-related physiology in the nervous system.

Imaging Tissue Composition: A Physics Viewpoint

While MRI stands out as a modality to characterize brain tissue *in vivo*, information on iron and myelin is obtained only indirectly. Before introducing specific methodological concepts, it seems useful to revisit some fundamental aspects.

Highlights

Emerging MRI techniques are progressing towards a means for the quantification of iron concentration or myelin content over the scale of a whole brain at submillimeter resolutions both *ex vivo* and *in vivo*.

Complementary techniques borrowed from analytical chemistry and solid-state physics can help in the specification and quantification of iron forms in the brain.

Multiparametric imaging approaches yielding quantitative information on both iron and myelin content may provide useful biomarkers to assess white matter integrity in clinical studies that use iron chelation therapy for diseases associated with iron deposition.

¹Max Planck Institute for Human Cognitive and Brain Sciences, Stephanstr. 1A, Leipzig, Germany

²Department of Radiology, C.J. Gorter Center for High Field MRI, Leiden University Medical Center, Leiden, The Netherlands

³Department of Neurosurgery, Pennsylvania State University College of Medicine, Hershey, PA, USA

⁴Université Catholique de Louvain, Louvain-la-Neuve, Belgium

⁵Department of Biomedical Engineering, Vanderbilt University, Nashville, TN, USA

⁶Centre for Neuroinflammation and Neurodegeneration, Department of Medicine, Hammersmith Hospital Campus, Imperial College London, London, UK

⁷Institute of Biomedical Technologies, National Research Council of Italy, Segrate, Milan, Italy



Box 1. Techniques to Measure Brain Iron Content Post Mortem

A detailed summary of earlier work measuring brain iron content and regional distribution of selected iron compounds, as well as MRI parameters, has been published by Haacke *et al.* [33]. Investigations of elemental concentrations and distributions of nanoparticulate compounds in postmortem brain tissue benefit from multimodal approaches in addition to conventional histology, such as classical Perls' Prussian blue staining or immunohistochemistry. Iron concentrations have been quantified by atomic absorption spectroscopy (AAS), inductively coupled plasma mass spectrometry (ICP-MS), or neutron activation analysis (NAA). Laser ablation ICP-MS and particle-induced X-ray emission (PIXE) yield quantitative chemical information about spatial distributions of elements and may be combined with focused beam synchrotron X-ray fluorescence (SXRF) analysis offering outstanding spatial resolution and specificity [110]. Mössbauer spectroscopy, electron paramagnetic resonance (EPR) spectroscopy, and superconducting quantum interference device (SQUID) magnetometry are more suitable for structural and/or physical characterization, but they also allow quantification when a proper reference compound is used [110,115,140].

Quantification of iron content in $\mu\text{g/g}$ wet tissue weight is appropriate for comparisons with MRI results; however, in the literature, concentrations are sometimes expressed in terms of dry weight or total protein weight. In this regard, the water content of brain tissue varies with age and in different brain regions (e.g., occipital cortex ~83–85%, frontal white matter ~67–72%, SN ~74%, putamen ~79–85%, caudate nucleus ~81–87%, and globus pallidus ~74%) and is also affected by health state [30,141]. Therefore, concentrations referring to wet weight are preferred. Fixation of tissues with formalin or other reagents can redistribute iron in the brain with possible alteration of staining intensity and may alter iron chemistry or the macromolecular state with possible effects on MRI [142]. Similarly, iron oxides may arise through postmortem redox reactions during sample preparation or exposure to high-energy probes during analysis and confound the results from other analytical techniques. Finally, dissections should be performed with non-iron blades to avoid further contamination [30,143].

⁸Department of Psychiatry, Columbia University Medical Center, New York State Psychiatric Institute, New York, NY, USA

*Correspondence: moeller@cbs.mpg.de (H.E. Möller).

Nuclear Precession, Relaxation, and the Most Abundant Biomolecule

MRI relies on the observation of the collective behavior of a vast number of nuclear magnetic dipoles. In a magnetic field, these dipoles execute a **precession** about the field axis at the **Larmor frequency**, which is directly proportional to B_0 (the magnetic field amplitude). At thermal equilibrium, the dipoles have a slight tendency to point along the field, yielding a small net **magnetization** of the sample parallel (i.e., **longitudinal**) to the field. For image acquisition, the magnetization is tilted away from this orientation by application of radiofrequency pulses to generate a **transverse** component. As the individual dipoles precess, so does the bulk magnetization, and the rotating transverse component induces an AC signal voltage in a receiver coil. The phase of the AC signal reflects the azimuthal angle of the precessing magnetization and allows measurement of the Larmor frequency (and, hence, B_0). Relaxation processes lead to a decay of the transverse magnetization and a re-establishment of the equilibrium longitudinal component with associated time constants T_2 and T_1 , respectively. They are often more conveniently expressed as relaxation rates, $R_2 = 1/T_2$ and $R_1 = 1/T_1$.

In biomedical MRI, the signal is typically obtained from hydrogen nuclei ('protons') in water molecules because they are by far the most abundant nuclear dipoles in tissues and also the most sensitive ones. Thus, the signal magnitude is proportional to the tissue water content. Yet, MRI is not limited to mapping the distribution of water. Interactions of the water protons with the surrounding matter impact their precession and relaxation, which can be measured [10]. In other words, the ubiquitous water in the tissue, can be used to probe other aspects of tissue composition.

Longitudinal relaxation and **transverse relaxation** of protons are primarily facilitated by weak dipolar fields generated by other nuclei (e.g., other protons) or by unpaired electrons in ions or molecular components. These dipolar fields fluctuate due to molecular motions. The transient transverse magnetization is additionally affected by static magnetic field variations. Spatial magnetic field variations imply that signal contributions from different positions have slightly different Larmor frequencies and progressively get out of sync (i.e., the net signal decays). Molecular motion reduces such dephasing because Larmor frequency differences average out if water molecules diffuse a distance that is comparable to the length scale of the field variation. Static field

inhomogeneities arise, for example, if the imaged object is nonuniformly magnetized due to the presence of compounds of different magnetic susceptibility. Here, a cellular spatial scale associated with the tissue microstructure is of particular interest. Taken together, the MRI signal decays away with an effective transverse relaxation rate $R_2^* = 1/T_2^*$ that comprises two terms [11]: (i) an irreversible contribution, $R_2 = 1/T_2$, due to dipole fields on a molecular length scale; and (ii) another contribution, $R_2' = 1/T_2'$, from field variations over longer distances.

As mentioned earlier, the phase of the MRI signal and its decay rate R_2^* reflect the mean and width of the intravoxel Larmor frequency distribution, respectively [12]. Both parameters can be mapped using gradient-echo pulse sequences. The transient signal can also be modeled for susceptibility distributions comprising objects of simple geometries (e.g., spheres to model cells or cylinders to model axons) [13]. Typically, water diffusion needs to be considered because it affects R_2^* [11,12,14].

Methodological Aspects of Susceptibility-Based MRI

One of the most prevalent uses of R_2^* -weighted MRI is blood oxygenation level-dependent (BOLD) functional imaging. It relies on the susceptibility difference between **diamagnetic** oxygenated and **paramagnetic** deoxygenated hemoglobin. The BOLD contrast may also be used for mapping venous vessel sizes [15] or oxygen extraction [16]. Both magnitude and phase information are combined in susceptibility-weighted imaging (SWI), which achieves, for example, the visualization of veins [17].

SWI uses the phase merely as a filter to enhance T_2^* -weighted images, whereas quantitative susceptibility mapping (QSM) uses it to reconstruct maps of the bulk susceptibility [18–20]. This involves solving the inverse source problem of the nonlocal B_0 variation induced by the susceptibility distribution [21].

For detailed discussions of QSM procedures, the reader is referred to a collection of excellent reviews [22–25]. Phase-based field mapping becomes increasingly attractive at higher fields. Optimum contrast is achieved at an echo time $TE \approx T_2^*$. However, given that the brain comprises tissue components with different T_2^* , multiple-echo acquisitions offer better flexibility. Whereas image acquisition is fairly straightforward, the reconstruction of susceptibility maps is a multistep procedure of substantial complexity (see Figure 1 in [25]). A plethora of algorithms have been developed to deal with various methodological considerations and caveats (e.g., multichannel phase combination, phase unwrapping, background phase removal, and regularization) [23–27].

Of note, sources other than susceptibility also impact phase contrast, such as magnetization exchange between water and macromolecules (see later) [28]. Another issue is that QSM provides only a relative measure of magnetizability. Absolute quantification requires a reference with known susceptibility [24].

Linking Susceptibility-Based Contrast to Iron

Both R_2^* and QSM provide sensitive measures of magnetic field perturbations. QSM can further distinguish whether the perturbation is due to diamagnetic or paramagnetic compounds. However, susceptibility-based contrast does not report on the chemical nature of perturbing particles. The link to iron relies on biological considerations: iron is by far the most abundant paramagnetic ion in the brain, whereas nonpathological concentrations of copper or manganese are too low to be detected [29,30]. Consistently, a linear correlation between R_2^* and iron concentrations was found in several brain areas of normal subjects [3]. Furthermore, recorded susceptibility maps resemble patterns from histological iron stains, particularly in deep GM (Figure 1A, Key Figure) [31]. Most brain iron (approximately two-thirds) is stored in ferritin (or hemosiderin) or, in the

Glossary

Astrocytes: star-shaped glial cells supporting BBB maintenance, provision of nutrients to neurons, tissue repair, and facilitation of neurotransmission.

Blood–brain barrier (BBB): vascular barrier resulting from tight junctions formed by endothelial cells of cerebral blood vessels; largest interface for blood–brain iron exchange.

Ceruloplasmin: multicopper ferroxidase existing as membrane-bound and soluble forms (e.g., in plasma and cerebrospinal fluid).

Choroid plexus: vascular tissue in the ventricles producing cerebrospinal fluid in the adult brain.

Diamagnetism: originates from induced currents in the electron cloud within an atom generating weak fields opposing an applied magnetic field.

Divalent metal transporter 1

(DMT1): major transmembrane transporter of divalent cations, such as Fe^{2+} , into cells and across endosomal membranes during the transferrin cycle.

Ferroportin: major iron exporter protein exporting Fe^{2+} out of cells; exported Fe^{2+} is oxidized by ferroportin-associated ferroxidases (e.g., hephaestin or ceruloplasmin).

Hephaestin: membrane-bound ferroxidase that oxidizes Fe^{2+} exported through ferroportin to Fe^{3+} that can then be bound to transport proteins.

Hepcidin: peptide secreted by the liver and possibly other cell types, controlling the amount of iron exported out of cells by ferroportin.

Labile iron pool (LIP): exchangeable pool of redox-active iron complexes of low stability within the cell.

Larmor frequency: precession frequency of nuclear spins (or the bulk net magnetization) in a magnetic field.

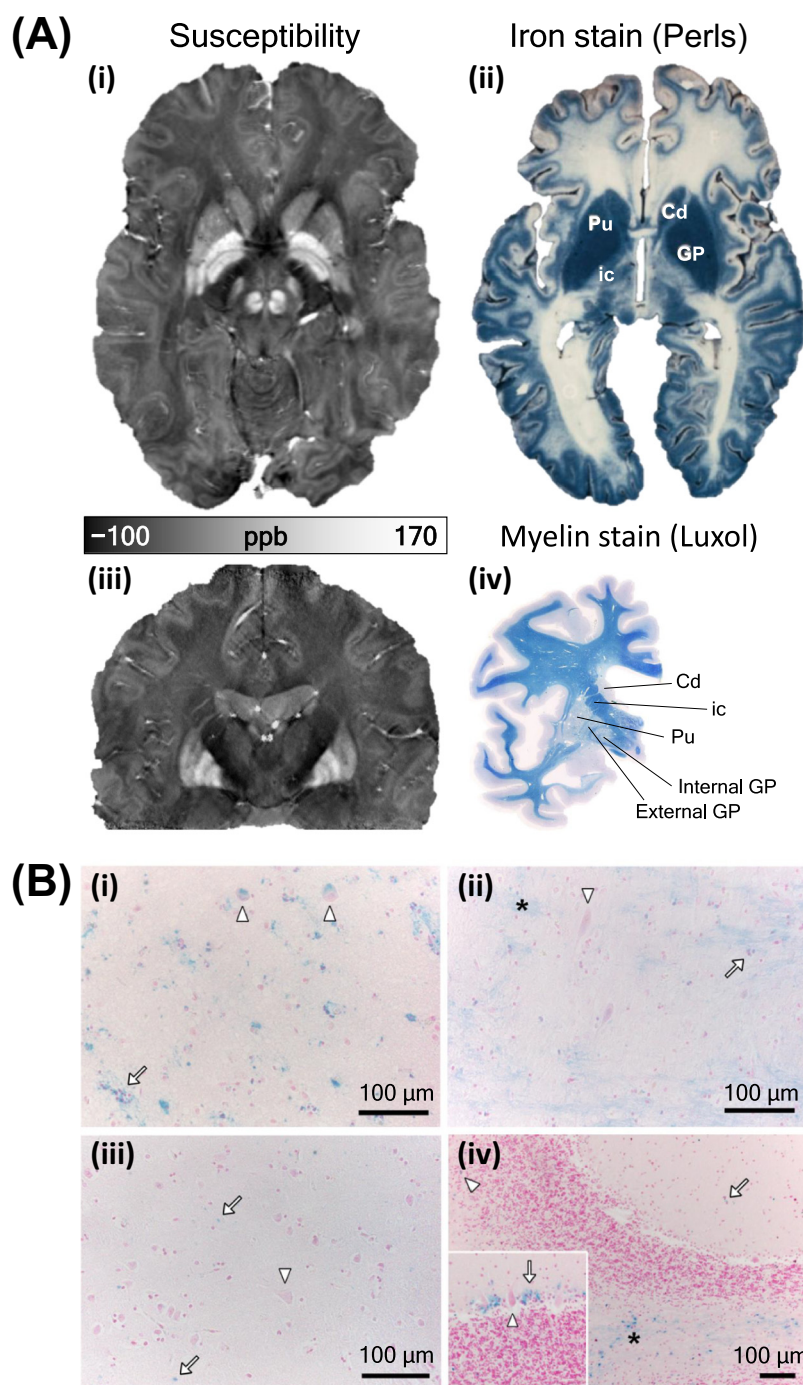
Longitudinal (magnetization): magnetization vector component parallel to the magnetic field.

Longitudinal relaxation: regeneration of longitudinal magnetization at a rate R_1 after perturbation of the thermal equilibrium.

Macrophage: type of white blood cell that participates in the immune response supporting either a pro- or anti-inflammatory tissue environment that depends on its cellular iron status; major roles include eliminating phagocytic particles, such as cellular debris or bacteria, and foreign substances.

Key Figure

3D Quantitative Susceptibility Mapping and Comparison with Histology



Trends in Neurosciences

(See figure legend at the bottom of the next page.)

Magnetic susceptibility: physical quantity that describes the magnetization of a material in response to an applied magnetic field; negative for diamagnetic and positive for paramagnetic, ferromagnetic, and ferrimagnetic substances.

Magnetization: density of (permanent or induced) magnetic dipole moments in a magnetic material; expresses the extent to which the material is 'magnetized'.

Magnetization transfer (MT): exchange of longitudinal magnetization between water and macromolecules.

Microglia: type of glial cell and the resident macrophages of the brain, thus subserving, in part, similar functions as macrophages.

Nontransferrin-bound iron (NTBI): part of iron (essentially low molecular weight one) that is not bound to transferrin.

Oligodendrocyte: type of neuroglia providing support and insulation to axons in the brain by creating the myelin sheath.

Paramagnetism: originates from spins of unpaired electrons, which tend to align parallel to an applied magnetic field.

Precession: rotational motion on a cone performed by the axis of a spinning object in response to an external torque.

Relaxation: re-establishment of thermal equilibrium after a perturbation.

Superparamagnetism: size-dependent form of magnetism typical of nanoparticles; characterized by collective spin dynamics driven by thermal fluctuations.

Transferrin (Tf): glycoprotein that binds two Fe^{3+} for transport and delivery to cells; iron-free and iron-loaded forms are apo- and holo-transferrin, respectively.

Transverse (magnetization): magnetization vector component perpendicular to the magnetic field; generates the MRI signal.

Transverse relaxation: leads to MRI signal decay at an effective rate $R_2^* = R_2 + R_2'$; fluctuating dipole fields produce irreversible signal loss (rate R_2), whereas static field inhomogeneities cause reversible loss (rate R_2').

Box 2. Main Iron Compounds in the Human Brain

Ferritins are ubiquitous oligomeric iron storage proteins, storing ferric iron (Fe^{3+}) in a water-soluble, nonreactive, bioavailable form. They are 24-subunit heteropolymers comprising variable amounts of two types of subunit, the heavy (H) and light (L) chain, forming a hollow protein shell that can store up to 4500 Fe^{3+} ions [1]. H-ferritin oxidizes ferrous iron (Fe^{2+}) to Fe^{3+} before storing, whereas L-ferritins lack ferroxidase activity and contribute to the nucleation of the iron core inside the protein. H-ferritins are mainly present in neurons, whereas L-ferritins are mainly expressed in microglia. Oligodendrocytes express a mixture of both subunits. Astrocytes in the resting brain have limited expression of ferritin [144].

Hemosiderin is formed after degradation of ferritin within lysosomes and principally contains Fe^{3+} and likely Fe^{2+} . Iron is more easily released from hemosiderin cores than from ferritins ([145] and references cited therein). Hemosiderin is formed in conditions of iron overload and accumulates in neurons and glia in aging (Figure 1B in the main text) [34,101] and diseased brains, such as in patients with AD, PD, progressive supranuclear palsy, and other neurodegenerative disorders [145] indicating a need for thorough brain-imaging studies.

Neuromelanin pigment comprises melanic, lipid, and protein components forming an insoluble compound contained in autolysosomal organelles [146]. Neuromelanin efficiently binds iron in neurons, but in such a way that neuromelanin-containing neurons do not have histochemically detectable iron deposits (Figure 1B in the main text) [34]. With Fe^{3+} , neuromelanin pigment forms two types of iron center, the mononuclear and multinuclear iron complexes. Both are of rhombic configuration but have different chemical and magnetic properties [34]. The amount of iron bound to neuromelanin varies with brain regions and type of neurons [105]. The neuromelanin-iron complex is abundant in catecholamine neurons of SN and locus coeruleus, but is also present, at lower concentrations, in other brain regions [105].

Nanoparticles of magnetite have been detected in human brain tissue and meninges [115]. Recently, spatial mapping of the magnetic fraction in the brain showed that residual magnetic compounds are present throughout the brain, with highest concentrations in the cerebellum and brain stem [118]. These particles are particularly interesting because they affect proton spin relaxation (and, hence, MRI contrast) and may promote neurotoxicity if Fe^{2+} is released from the mineral. Whether such particles result from pathological ferritins [145], ferrihydrite interacting with β -amyloid [109] or possibly airborne particulate matter [117] is currently an issue of debate.

case of dopaminergic neurons, in neuromelanin (Box 2) [1,32–34]. These compounds contain thousands of Fe^{3+} ions, mainly as clusters, and have strong **superparamagnetic** susceptibilities (Box 3) making them effective field perturbers [14,35]. Brain levels of **transferrin** (Tf), the major iron transport protein, are only one-tenth of ferritin levels and probably insufficient for a relevant effect on susceptibility-based MRI contrast [29,33]. Total concentrations of low-molecular-weight iron complexes (see later) are even lower [1,29]. Notably, hemoglobin does not significantly affect phase contrast between GM and WM [36].

Susceptibility heterogeneity in WM indicates relevant contributions from diamagnetic myelin in addition to those from paramagnetic iron [7]. This is in line with the observation that correlations between QSM and putative iron storage concentrations improve after correction for myelin [20].

Figure 1. (A) Gradient-echo imaging at 7 T *in vivo* [31] showing transverse (i) and coronal sections (iii) of the susceptibility distribution difference from value in frontal deep white matter (WM) at the level of the basal ganglia, and histochemical staining for ferric iron [(ii) Perls' Prussian blue] [2] and myelin [(iv) Luxol fast blue, left hemisphere] in two other fixed human brains. Iron-rich regions in putamen (Pu), globus pallidus (GP), and caudate (Cd) [greatest blue intensity in (ii)] show large positive susceptibility shifts, whereas the myelin-rich internal capsule (ic) [dark-blue staining in (iv)] shows a negative susceptibility shift. (B) Iron deposits visualized by Perls' histochemistry: Pu (i) and GP (ii) of a 71-year-old healthy subject have abundant iron deposits in whole parenchyma, mainly in glia (blue staining, arrows) and fibers [asterisk in (ii)]. Iron deposits are detected in cytoplasm of neuromelanin-free neurons [arrowheads in (i) and (ii)], whereas neuromelanin-containing neurons do not have reactive iron deposits (not shown) [34]. Premotor cortex (iii) of a 72-year-old subject shows fewer iron deposits, mainly in glia (arrows) while generally absent in neurons (arrowhead). In cerebellum of an 80-year-old subject (iv), iron deposits are scattered among molecular layer (arrow), granular layer (arrowhead), and WM (asterisk) with most intense staining. Iron deposits are sometimes observed between molecular and granular layers (arrow in inset), while Purkinje cells (arrowhead in inset) do not appear to contain reactive iron deposits. Reproduced, with permission, from [2] (Aii). Adapted, with permission, from [31] (Ai) and [34] (B). Coronal susceptibility map (Aiii) and myelin stain (Aiv) courtesy of Andreas Schäfer and Markus Morawski, respectively.

Box 3. Magnetic Properties of Iron Compounds

The nanomineral ferrihydrite ($\text{Fe}_2^{\text{III}}\text{O}_3 \cdot 0.5\text{H}_2\text{O}$) is present in the core of ferritin and hemosiderin deposits. The magnetic properties of this hydrous ferric oxyhydroxide are still under discussion. However, it is generally accepted that the ferritin core is antiferromagnetic [147] and the presence of uncompensated spins in its core or on the surface lead to a net magnetic moment of ~ 300 Bohr magnetons (μ_B) per particle [148]. Due to the presence of a 2 nm-thick shell, ferritins behave like noninteracting superparamagnets. Ferritin magnetization and transverse relaxivity are approximately two orders of magnitude lower than those of magnetite and are strongly field dependent [148]. In fact, ferritin magnetization does not saturate up to very high fields, due to surface spin-canting [147–149]. Ferritin relaxivity can be described only by combining different mechanisms: the outer-sphere and proton-exchange mechanisms.

In neuromelanin pigment, high-spin Fe^{3+} ($S=5/2$) is bound to oxygen atoms of catechol groups in mononuclear complexes, whereas, in multinuclear complexes, low-spin Fe^{3+} ($S=1/2$) forms oxy-hydroxy aggregates [34]. Neuromelanin leads to paramagnetic T_1 -shortening effects when combined with iron, as a result of the dipolar fields generated by the metal and the fast exchange between water molecules and hydroxide ligands on the iron [131]. Additionally, neuromelanin significantly affects the T_2 relaxation and tissue susceptibility [150].

Magnetite ($\text{Fe}^{\text{II}}\text{Fe}_2^{\text{III}}\text{O}_4$) is a ferrimagnet with net magnetic moment of $\sim 4 \mu_B$ per formula unit resulting from competing ferromagnetic coupling between Fe^{3+} and Fe^{2+} spins on octahedral lattice sites, and antiferromagnetic coupling between Fe^{3+} spins on octahedral and tetrahedral sites. Magnetite nanoparticles in the brain are superparamagnetic at room temperature due to their small size (median ~ 20 nm) [117]. At fields typical of MRI experiments, magnetite displays a large magnetization in the range of 80–90 A m²/kg depending on the particle size [151]. In the vicinity of the particles, transverse proton relaxation is greatly enhanced, as described by the outer-sphere mechanism [149].

Maghemite ($\gamma\text{-Fe}_2^{\text{III}}\text{O}_3$) is another iron oxide that can be considered as Fe^{2+} -deficient magnetite (vacancies on octahedral lattice sites). It is also ferrimagnetic and shows magnetic and structural properties similar to magnetite. Therefore, it is often difficult to distinguish between the two forms. Both maghemite and magnetite have been found in the core of ferritins obtained from pathological tissue [145].

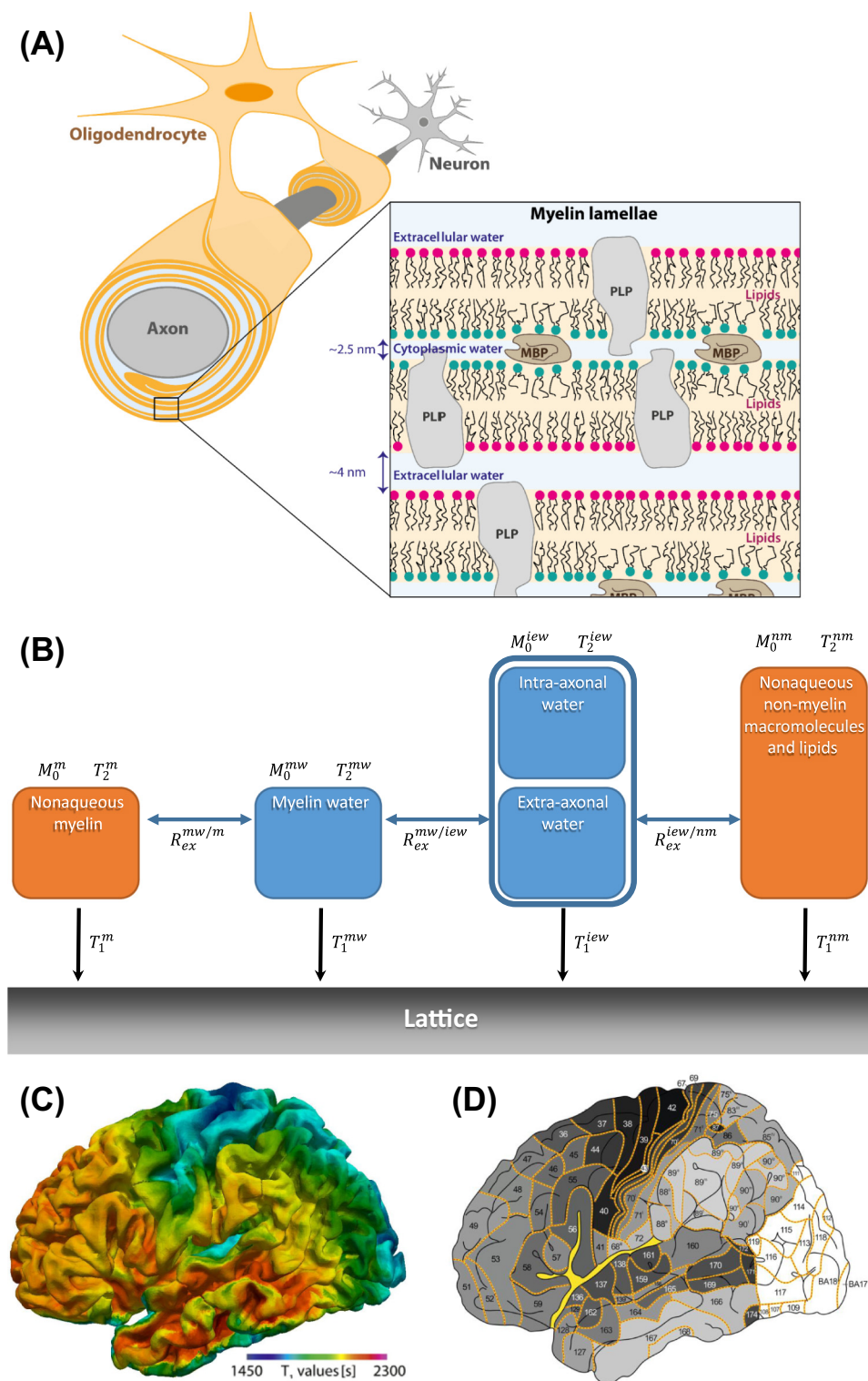
It is now established that, mainly due to iron (Box 3), GM exhibits a paramagnetic shift of the susceptibility compared with water [14]. WM shows a diamagnetic shift and anisotropy related to the ordered arrangement of lipids in myelin membranes (Figure 2A) [19,23,37]. Given that a scalar quantity does not capture anisotropy, a susceptibility tensor has been introduced as a more appropriate metric in WM and was shown to achieve delineation of fiber tracts [38].

Myelin-Sensitive MRI Based on Relaxation

Given that both iron and myelin affect tissue magnetic susceptibility, further information is required to disentangle both contributions. Therefore, here we discuss relaxometry techniques that are sensitive to myelination, along with underlying model assumptions. In doing so, it should be kept in mind that R_1 , R_2 , and R_2^* are not only affected by myelin, but also by iron or other compounds [4].

In the confined environment between adjacent myelin membrane layers (Figure 2A), water protons experience frequent interactions with nonaqueous components. This accelerates transverse and longitudinal relaxation [39] and induces magnetization exchange between water and macromolecular protons (via crossrelaxation or chemical exchange), commonly referred to as **magnetization transfer (MT)** [40]. Each of these factors can contribute MRI contrast that reports on myelin content. Experimental studies have aimed to model the role of myelin, but some details remain elusive [41–43]. A model of WM comprising only three microanatomical compartments (Figure 2B) is already too complex (regarding the number of model parameters) for clinically practical MRI. Instead, the role of myelin is best appreciated in terms of simpler models.

For measurements of R_2 or R_2^* , a common simplification is to ignore macromolecular protons and consider the intra- and extra-axonal space as one compartment that does not significantly exchange water with the myelin compartment. The myelin-water signal fraction (MWF) can then be distinguished from intra- and/or extra-axonal water signals by multiexponential R_2 [44–46] or



(See figure legend at the bottom of the next page.)

multiexponential R_2^* analysis [47,48]. Multiple studies support the conclusion that MWF is a correlative measure of myelin content [49,50]. For either R_2 or R_2^* , signal-to-noise ratio (SNR) requirements are high. Furthermore, the assumption of no water exchange between myelin and intra- and/or extra-axonal spaces may not always hold, in particular, in smaller axons with thinner myelin. This may result in underestimation of myelin content [51–53] and an axon size-dependent MWF estimate.

The same simplified model may be applied to measurement of R_1 , allowing MWF estimation by multiexponential analysis of longitudinal relaxation [54]. This approach suffers the same SNR and water-exchange challenges as discussed earlier. It may also suffer from inaccuracy due to MT with the macromolecular proton pool [43,55–57], which cannot, in general, be ignored for longitudinal relaxation. From a pragmatic perspective, this confound may not be a practical problem because MT is also dependent upon myelin.

For this reason, MT contrast may be directly used to measure myelination. Although myelin is not the only source of MT (e.g., other cell membranes also exchange magnetization with water), myelination has been shown to correlate with MT contrast [58]. Quantitative measures of MT can be achieved via different pulse sequences [10,56,59–61]. Another approach is to assume that MT is the dominant factor contributing to a measure of R_1 [4,62]. Consequently, even appropriately calibrated T_1 -contrast may provide sufficient semiquantitative information on myelination [63,64]. Although an oversimplification, this model has gained popularity as a fast, high-resolution approach to myelin mapping, particularly in cortex (Figure 2C,D) [65]. However, the above models were developed for WM, whereas GM, with its characteristic layer structure and lower myelin content, may differ in its MR behavior.

There is presently no single approach for relating MRI measures to myelin content that is decidedly better than others. Multiexponential R_2 and quantitative MT likely use the best-founded models. R_1 measures, although perhaps less specific to myelin, offer faster acquisitions, higher resolution, and lower specific absorption rates.

From Biomarkers to Neurobiology

So far, we have discussed how MRI provides biomarkers of tissue properties in terms of physical parameters (e.g., susceptibilities, relaxation rates, and MT parameters). These biomarkers are quantitative in the context of physical signal models, which make simplifying assumptions about compartmentation or exchange. Given that they are sensitive to multiple substrates

Figure 2. Impact of Myelination on Proton Relaxation. (A) The brain myelin sheath comprises tightly wrapped layers of oligodendrocyte cell membranes, with water residing in thin spaces between adjacent layers. Myelin water content is relatively low (approximately half that in other soft tissue), water mobility is reduced [152], and water proton relaxation is accelerated [39]. Macromolecular protons are typically not directly observed due to extremely short T_2 , but affect water magnetization through magnetization transfer (MT) [40]. The ordered arrangement of elongated lipid molecules leads to radial anisotropy of the susceptibility of myelin [37] and orientation dependence of its dipole-broadened lineshape [57]. (B) Model of water protons considering intra-axonal (axoplasm), extra-axonal (space in between axons), and myelin compartments. Including macromolecular protons leads to five or six proton pools with MT between water and macromolecules and intercompartmental water exchange as coupling pathways. In white matter (WM), intra- and extra-axonal water are typically indistinguishable by relaxometry, and a four-pool model is appropriate [42,43]. (C) Average T_1 at 7 T across cortical depth in ten healthy subjects displayed on the midsagittal surface [153] and (D) cortical density of myelinated fibers (without data for insular and occipital cortices) [154], both coregistered to the Colin27 brain atlas (<https://doi.org/10.6084/m9.figshare.4834004.v1>). Areas of higher myelination [dark gray in (D)] show shorter T_1 values [blue to green colors in (C)]. Abbreviations: iaw, intra-extra-axonal water; M_0 , equilibrium magnetization; MBP, myelin basic protein; m, myelin; mw, myelin water; nm, non-myelin; PLP, proteolipid protein; R_{ex} , magnetization-exchange rate; T_1 , longitudinal relaxation time; T_2 , transverse relaxation time. Reproduced, with permission, from [154] (D). Adapted, with permission, from [155,156] (A) and [42] (B). T_1 map rendering (C) courtesy of Pierre-Louis Bazin.

(e.g., iron, myelin, and water content), there is increasing interest in multiparametric imaging strategies [66,67]. Data-driven approaches (e.g., independent component analysis and machine learning) may be used to improve the biological specificity of the combined images [68]. Biophysical forward models aim to compute the contrast induced by selected tissue properties (e.g., iron and myelin distributions) [69]. However, model inversion to estimate concentrations from the MRI data is complicated and typically ambiguous. A crucial step in this process is *ex vivo* validation using complementary techniques reporting on tissue composition (Box 1). Further refinement of biophysical models is important to account for different molecular forms of iron and their inhomogeneous distribution among cell types and subcellular compartments (see later). These are topics of current neuroimaging research that require the participation of biologists. While MRI offers a view on tissue composition *in vivo*, it remains, from a biological perspective, to integrate obtained information on iron deposits (e.g., iron storage) into concepts of iron homeostasis and transport as well as alterations related to development and/or aging or disease.

A Global View of Human Iron Biology

Cellular iron biology involves uptake of iron into a low-molecular-weight cytosolic pool of indeterminate composition, designated the '**labile iron pool**' (LIP), and its use for the metalation of iron-containing proteins, storage in the ubiquitous iron storage protein ferritin and export (e.g., Figure 3 in [70]) [1]. In most cells of the body, iron homeostasis is regulated at the level of the translation or stabilization of mRNAs by iron-regulatory proteins (IRPs; e.g., Figure 4 in [70]). In conditions of iron insufficiency, IRPs bind to *cis*-regulatory RNA hairpin structures (iron-regulatory elements, IREs) present in the 5'- and 3'-untranslated regions of mRNAs. Consequently, synthesis of proteins of iron storage, export, and utilization is prevented, whereas cellular uptake from circulating Tf increases, thereby increasing the intracellular iron level in the LIP. Once this level reaches a tipping point or, in the case of iron excess, the IRPs lose their capacity to bind to the IREs, and the storage, export, and use proteins are now synthesized, whereas Tf mRNA is degraded. Thus, 'iron controls iron' [71], the level of LIP acting as a trigger, switching the IRE-IRP system between its two states to fine-tune intracellular iron metabolism.

Systemic iron homeostasis involves the hepcidin-**ferroportin** axis, which coordinates iron export into the bloodstream from duodenal enterocytes, **macrophages** involved in iron recycling from effete red blood cells, and periportal hepatocytes, through the interaction between the transmembrane export protein ferroportin and **hepcidin**. Hepcidin is synthesized and secreted by the liver, and its expression is regulated by iron status, erythropoietic demand, inflammation, and other factors [72]. Binding of hepcidin triggers ubiquitination of lysine residues in ferroportin, accompanied by its endocytosis, internalization, and degradation, thereby abolishing iron export. When hepcidin synthesis stops, ferroportin can once again resume iron exportation.

Iron Biology and the Brain

Brain iron transport is illustrated in Figure 3. Iron transport across the **blood-brain barrier (BBB)** involves Tf uptake through the brain capillary endothelial cells, probably by the classic transferrin-to-cell cycle [73,74]. Once iron has been released into the LIP, apo-Tf is recycled back to the luminal membrane, where it is released. Ferrous iron (Fe^{2+}) is transported out of the endothelial cell at the abluminal membrane into the interstitial fluid (ISF) by ferroportin. Fe^{2+} in the ISF can be oxidized to Fe^{3+} by membrane-bound **ceruloplasmin** or **hephaestin**, and by soluble ceruloplasmin secreted from pericytes and **astrocytes** [74]. Fe^{3+} can then enter brain cells in the form of complexes with citrate, ATP or ascorbate (**nontransferrin-bound iron, NTBI**), which astrocytes secrete, or by other mechanisms as reviewed by Ward *et al.* [75]. Fe^{3+} can also be incorporated into Tf, secreted into the ISF by the **choroid plexus**.

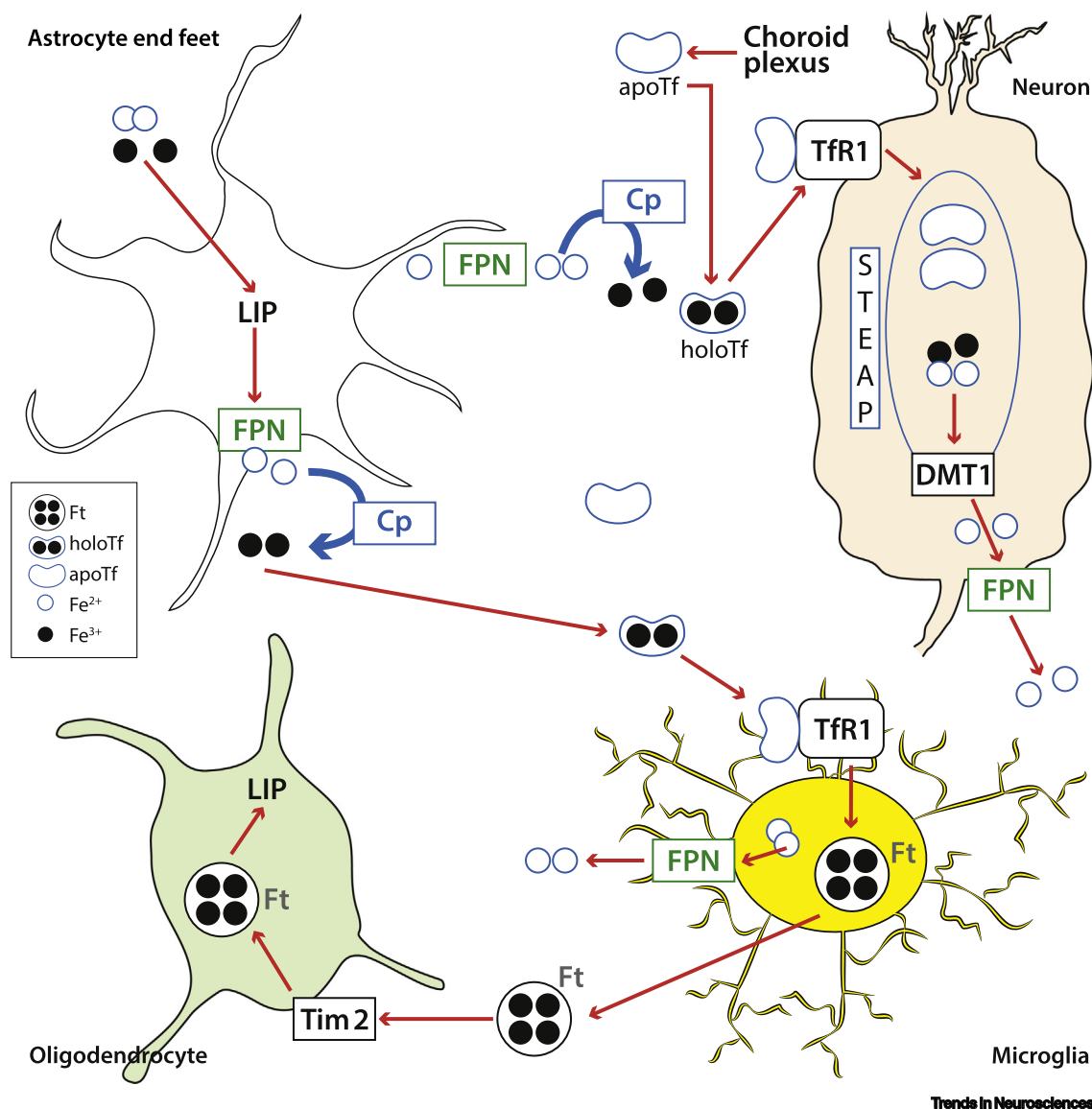


Figure 3. Iron Transport in Brain. From top left: Once iron (open and filled circles indicate ferrous and ferric iron, respectively) has been released from brain capillary endothelial cells, it is taken up by the perivascular end feet of astrocytes. The astrocytes then release Fe²⁺ via ferroportin (FPN), which can be oxidized by ceruloplasmin (Cp), and incorporated into apo-transferrin (apoTf), which can then be taken up by neurons and microglia. This involves the classic transferrin-to-cell cycle involving STEAP reductases and divalent metal transporter 1 (DMT1). Oligodendrocytes may take up iron from ferritin (Ft) released into the interstitial fluid from microglia, via T cell immunoglobulin and mucin domain-containing protein 2 (Tim2). Abbreviations: holoTf, holo-transferrin; LIP, labile iron pool; TfR1, transferrin receptor 1.

Iron in Different Brain Cell Types

Neurons take up iron, essentially from Tf through transferrin-receptor (TfR)-mediated endocytosis, and export excess iron via ferroportin (Figure 3) [75]. In common with neuroglia, neuronal iron from the cytosolic LIP can be stored in ferritin or used for the metalation of iron-containing proteins. Astrocytes take up NTBI from the BBB as indicated above. **Microglia** have been reported to have both TfRs and ferroportin [76]. The main iron-containing cells in the adult brain are **oligodendrocytes**, although, during brain development, microglia are the first to stain for iron as ferritin, with iron staining shifting subsequently to oligodendrocytes [77]. The mechanism

by which mature oligodendrocytes acquire iron was somewhat of a conundrum for many years because they do not express TfRs. Recently, H-ferritin was demonstrated to provide iron to these cells in both rodents [78] and humans [79]. Expression of ferritin by various brain cell types is strong indirect evidence that they all contain sufficient intracellular iron to require storage.

Regulation of Brain Iron Homeostasis and Influences of Inflammation

Regulation of brain iron homeostasis at the cellular level clearly involves IRPs and their regulation of TfR1 and ferritin. IRP2 deficiency causes iron dysregulation in the brain [80,81] but the results are inconsistent and impact on myelination appears minimal. As mentioned earlier, mutations in **divalent metal transporter 1 (DMT1)** result in significant disruption of iron homeostasis, including loss of myelin [82]. It is currently unclear whether hepcidin has a key role in brain iron homeostasis, whether it is synthesized locally in the brain by specific cells, or whether hepcidin is able to cross the BBB after synthesis in the liver. These questions remain to be addressed.

After an inflammatory stimulus, expression of hepcidin in astrocytes and microglia increases, but not so in neurons. In addition, expression of DMT1 increases, whereas expression of ferroportin 1 decreases, in all three cell types [83]. The net result is increased iron accumulation in neurons and microglia but not in astrocytes. Recently, a model was proposed whereby inflammation initiates an intercellular signaling cascade in which activated microglia stimulate astrocytes to release hepcidin that, in turn, signals to neurons preventing their iron release and resulting in neuronal death [84]. In normal circumstances, in the adult brain, microglia are in a nonactivated state, displaying a ramified morphology. When abnormalities are detected, a sequence of events is set in motion, which results in an amoeboid microglia phenotype and leads to the release of both pro- and anti-inflammatory cytokines.

Iron Biochemistry Related to Myelin

Iron Acquisition and Distribution in Oligodendrocytes

Iron-stained oligodendrocytes are found both in GM and WM. Although oligodendrocytes in WM tracts are distributed uniformly, those that are iron positive occur in patches of varying sizes [85,86]. These patches are possibly associated with blood vessels running through the WM [85]. Oligodendrocytes that stain for Tf or ferritin appear uniformly in the WM, albeit aligned in rows [85,87].

The reason why oligodendrocytes are the predominant cell type to stain for iron is likely a combination of their high rate of metabolism [88] associated with the production and maintenance of myelin and their relatively minimal somatic cytoplasm. Iron accumulation by oligodendrocytes is not dependent upon the structural integrity of myelin [87]. If oligodendrocyte development is compromised, iron accumulates in astrocytes and microglia.

Role of Iron in Oligodendrocyte Biochemistry and Myelin Production

Functionally, iron is required for the activity of many enzymes related to the production and maintenance of myelin. One of the most prominent consequences of iron deficiency during postnatal development is hypomyelination. Peak iron uptake into the brain occurs at the time of peak myelination [89]. There are multiple examples of studies in iron-deficient children demonstrating increased latency of evoked potentials, which is interpreted as insufficient myelination. Here, iron- and myelin-specific MRI acquisitions would be particularly valuable. Decreased iron availability in rodents induces decreased expression of myelin proteins, lipids, and cholesterol [90–92]. Although none of the integral myelin proteins have been reported to be directly regulated by iron, the number of iron-dependent enzymes that are uniquely expressed or enriched in oligodendrocytes is extensive [85]. Lipid synthesis and breakdown is also iron dependent [93].

The role of iron in supporting general oligodendrocyte metabolic activity is frequently overlooked. Part of the reason could be a lack of appreciation for the distinction between the biochemical iron requirements of oligodendrocytes versus myelin production. Given that oligodendrocytes depend on iron for their function, clinical studies that use iron chelation therapy for diseases associated with iron deposition should monitor WM changes. Again, this hints at a need for multiparametric MRI to assess both iron and myelin. A number of these diseases already report apparent hypomyelination [94,95], and further decline of WM integrity will impact the functional outcomes since myelin integrity impacts movement and cognition.

There have been several studies on genetic mutations involving neurodegeneration and brain iron deposition, and these are typically associated with abnormal myelin metabolism [96]. For example, a mutation in the *HFE* gene, which results in increased overall iron accumulation, is associated with a myelin decrease in both mice and humans, indicated by R_2 [97,98], which may suggest decreased cholesterol in myelin. While early experiments indicated a particular sensitivity of proton relaxation to the cholesterol content of a membrane [6], it is unknown how an altered lipid composition of myelin may affect relaxation-based MRI. Myelin accounts for 80% of the brain cholesterol content [99] and is decreased in experimental models of *HFE* gene variants [97]. Another animal model that has shown disruptions in the MRI appearance of myelin is the Belgrade rat, which has a mutation in the *DMT1* gene resulting in decreased iron availability. Myelin composition has not been directly assessed, but iron staining in WM is markedly reduced, although still associated with oligodendrocytes, and the association of iron-positive oligodendrocytes and WM blood vessels is prominent [82]. Disruptions in WM and iron deposition in both humans and animals have also been reported in mucopolipidoses, which are a group of inherited metabolic diseases that affect lysosomal function [100].

Brain Iron Accumulation in Aging and Neurodegeneration

Highest concentrations of total iron are found in brain motor regions, including putamen, globus pallidus, caudate nucleus, cortices, and substantia nigra (SN) [75,101,102]. Aging is associated with an increased accumulation of iron in the brain, and recent QSM studies showed significant increases of iron in caudate, putamen, nucleus accumbens, and globus pallidus [103]. Levels of specific iron compounds increase with age, including H-ferritin in motor regions and frontal cortex, L-ferritin in SN and globus pallidus [101,104], and neuromelanin with a variable amount of bound iron (Figure 1B) [105]. There are many brain regions in which the age-related changes of the mentioned iron compounds are still unknown. The availability of these data would provide a necessary baseline for understanding MRI changes. To investigate the role of iron compounds in disease conditions, there is a need for longitudinal studies of healthy aging to detect early changes of iron compounds in subjects who may later develop the disease.

Some of these iron changes are associated with an increased risk of neurodegeneration, and a hallmark feature of most neurodegenerative diseases is the accumulation of total iron and LIP in specific brain regions [75,106]. Within these regions, there is neuronal loss caused by multiple factors, including iron-induced free radical damage, inflammation, protein misfolding and/or aggregation, or mitochondrial dysfunction. Examples include Huntington's disease, Friedreich's ataxia, as well as pantothenate kinase-associated neurodegeneration, aceruloplasminemia, and neuroferritinopathy with mutations in genes encoding proteins of iron metabolism. Here, we briefly present iron involvement in three major neurodegenerative diseases [Alzheimer's disease (AD), Parkinson's disease (PD) and multiple sclerosis (MS)], where the pathogenesis is mostly of a nongenetic type.

Alzheimer's Disease

AD is an age-related neurodegenerative disease, resulting in cognitive decline, memory loss, and changes in personality and behavior. Characteristic histopathological signs are the β -amyloid peptide deposited extracellularly as amyloid plaques, and the protein tau in the form of intracellular neurofibrillary tangles. Pathologically, iron is abundantly present in amyloid plaques and neurofibrillary tangles [107,108]. The exact forms of plaque-associated iron *in vivo* are not yet fully understood. *In vitro* studies suggest the ability of β -amyloid to reduce ferrihydrite [109] and the presence of ferritin core-sized nanoparticles with a magnetite and/or maghemite structure [110]. Localized accumulation of iron might deprive other brain areas of this metal, thus impairing neuronal function. H- and L-ferritin concentrations are decreased in frontal cortex, putamen, SN, and globus pallidus of patients with AD compared with controls [104]. Iron and ferritin contents increase in temporal cortex of patients with AD; however, iron loading of ferritins from cortex is similar in patients with AD and normal subjects [111]. In AD temporal cortex, the iron concentration is higher compared with controls and, in hippocampus, reactive iron is histochemically found [112]. Recently, QSM measures of iron accumulation have been linked to faster cognitive decline in patients with AD [113].

A systematic meta-analysis identified eight regions (including the temporal, parietal, and frontal lobes) of increased iron accumulation [114], also consistent with laser-ablation inductively coupled plasma mass spectrometry (ICP-MS) data [85]. Forms of iron include ferrihydrite, encapsulated within ferritin, and small amounts of magnetite (which is readily sensed by QSM), ~1% of total iron present, which may vary substantially among patients (Boxes 1–3) [111,115–118]. The importance of the formation of Fe^{2+} -rich, redox-active species leading to a sustained source of reactive oxygen species awaits clarification. Neuroinflammation may be an important source of brain iron by activating microglia increasing their intracellular ferritin content, mainly as L-ferritin [119].

In AD, there is an early loss of noradrenaline neurons containing neuromelanin in locus coeruleus that contributes to the mentioned symptoms [120], and MRI has shown corresponding loss of neuromelanin [121]. In principle, iron compounds in the locus coeruleus could be involved in neurodegeneration, but data on these compounds have been reported only for healthy aging [101]. Postmortem and *in vivo* investigations are needed to establish a possible role of iron compounds in locus coeruleus neurodegeneration during AD.

Parkinson's Disease

PD is the second-most common form of neurodegenerative disorder, mainly characterized by progressive loss of dopaminergic neurons in the SN pars compacta in the ventral midbrain and an approximately twofold increase in total iron accumulation. As disease severity increases, so does the total iron content in SN pars compacta and pars reticulata, which correlates with motor disability [122]. However, it is unknown whether the worsening of symptoms is related to alterations in ferritin, neuromelanin, or LIP. Therefore, dedicated studies are required to recognize whether these iron compounds may be suitable therapeutic targets. H- and L-ferritin decrease in the frontal cortex, SN, and globus pallidus compared with controls [104]. The simultaneous increase of total iron but decrease of ferritin in the SN of patients with PD are indicative of high iron loading of ferritins and/or increased LIP. The concentration of neuromelanin-iron complex decreases in the SN of patients with PD due to selective degeneration of neuromelanin-containing dopaminergic neurons. Here, neuromelanin has an increased iron load, and part of this iron is redox active [123]. However, in PD, the redistribution of excess iron between the different iron storage molecules deserves further studies. Plausible explanations for iron accumulation include BBB dysfunction, increased BBB permeability, activation of glia cells altering iron homeostasis, altered iron transport via specific receptors and/or transporters, or mutations related to iron

transport and binding proteins. Increased expression of DMT1 may contribute to PD pathogenesis via its capacity to transport Fe^{2+} [75]. A characteristic histopathological sign are Lewy bodies inside neurons, comprising aggregated α -synuclein (and other proteins), within which redox-active iron may accumulate [75]. Studies of the temporal cortex revealed a reduced iron content [124], as well as in the globus pallidus of patients with PD [122]. Intense microgliosis (i.e., neuroinflammation) occurs around extraneuronal neuromelanin (released by dying neurons) in the SN [125], which could be an important factor for increasing LIP content.

In healthy subjects, the neuromelanin-iron complex impacts MRI contrast mainly in the SN. In the SN of patients with PD, researchers observed a decrease in the neuromelanin-iron complex due to loss of catecholamine-pigmented (dopaminergic) neurons, together with the increase of total iron levels [122,126]. Indeed, loss of neuromelanin in the SN with associated loss in the ability to sequester iron might be characteristic for PD and detectable by MRI [127]. Neuromelanin-sensitive T_1 -weighted MRI showed diminished signal intensity in the SN of patients with PD [128] and reduced contrast in late-stage compared with *de novo* PD [129]. To date, no quantitative relationship between T_1 and the loss of neuromelanin and/or neurons has been established. Hence, *ex vivo* experiments in the SN of patients with PD to correlate T_1 and the content of neuromelanin-iron complex need to be designed to evaluate this relationship. An initial clinical trial using T_2^* as a biomarker showed that removal of iron by iron chelators from specific brain regions improved PD symptomatology [130]. The paramagnetic properties of neuromelanin-iron complex, due to its association with metals such as iron, induce T_1 shortening [131]; hence, the measurement of neuromelanin-sensitive contrast in the SN could be a useful diagnostic biomarker in neurodegenerative diseases, such as PD.

Multiple Sclerosis

In MS, the myelin sheath becomes damaged, impairing brain and spinal cord functions. Relaxometry and MT have been extensively used to investigate MS, in particular myelin integrity (e.g., [49,58,132,133]). This important field of research is beyond the scope of the current review. In terms of iron-related dysregulation, abnormally high iron levels in MS occur concomitantly in multiple deep GM structures, and in WM with pathological deposits of reactive iron and ferritins in microglia and oligodendrocytes usually located at sites of inflammation near blood vessels. A release of iron from degenerating oligodendrocytes that is accumulated into microglia and macrophages also occurs [134,135]. The mechanisms of abnormal iron deposition are not fully understood. It is also unclear whether such deposits have adverse consequences and contribute to pathogenesis. Iron of unknown speciation can accumulate in mitochondria, microglia, macrophages, neuropils, and neurons. Studies aimed to characterize the iron compounds and their amount accumulating in compartments of different brain cells are a prerequisite to investigate their role in the pathogenesis of MS and for the interpretation of MRI results. Iron accumulation is likely due to inflammation, increased BBB permeability, and penetration of iron-rich macrophages into parenchyma.

Concluding Remarks and Future Perspectives

MRI has matured over the past few years allowing *in vivo* assessment of brain iron levels and myelination. It is the modality of choice for investigating neurodegenerative disorders associated with iron accumulation [1]. Optimizing and standardizing acquisition protocols across magnetic field strengths and vendor platforms as well as image processing software will be essential for obtaining more robust biomarkers (see Outstanding Questions). A recent systematic comparison of 27 different QSM pipelines [136] is a step forward in this direction. Understanding MRI results may benefit from the integration of transcriptional information [137]. Genetically controlled selective uptake of ferritin or superparamagnetic magnetoferritin is another exciting line of research that allows tailored contrast manipulation on a cellular level [138,139]. To improve diagnosis and

Outstanding Questions

What are the sources of variation in estimates of cellular iron content obtained with different biophysical modalities?

What are the molecular forms of iron that are seen by quantitative MRI techniques?

How does an altered cellular distribution of iron due to disease impact the results obtained using quantitative MRI?

How does an altered lipid composition of myelin impact the results obtained using quantitative MRI?

Do all relaxation-based measures of myelin reflect the total amount of myelin? Do the number of myelin lamellae, axon diameter, or iron content affect relaxation-based measures of myelin?

How can MRI measures of tissue composition recorded in a fixed specimen *ex vivo* be converted to an *in vivo* scenario given the substantial differences between the two conditions in terms of their molecular dynamics, water exchange, or fixation-related structural and metal content alterations?

What is the role of inflammation in alterations in cellular iron distribution and initiation of accumulation of reactive and soluble or insoluble molecular forms of cellular iron?

How does inflammation interfere with the MRI signal attributable to iron or myelin?

Is the increased iron concentration observed in neurodegenerative diseases an effect of iron redistribution in the brain?

therapy monitoring, better specificity for different molecular species of iron and their cellular distribution is a goal for the future development of MRI methods. Inevitably, attempts to link neuroimaging findings to neurobiology will be an interdisciplinary enterprise.

Acknowledgments

This review was initiated by the Workshop 'Iron, Myelin and the Brain', held at the Lorentz Center, Leiden, The Netherlands on 12–16 March 2018, and tremendously benefited from committed discussions among the attendees (www.lorentzcenter.nl/c/web/2018/974/participants.php?wsid=974&venue=Oort). We would like to extend our appreciation to Andreas Schäfer, Jürgen Reichenbach, G. Allan Johnson, Markus Morawski, Pierre-Louis Bazin, and Rudolf Nieuwenhuys for kindly sharing imaging and histology data and to Heike Schmidt-Duerstedt for artwork. L.Z. and F.A.Z. thank the Section of Legal Medicine and Insurances, Department of Biomedical Sciences for Health at University of Milano for providing brain tissue samples. This work was supported by The Netherlands Organization for Scientific Research (NWO), through a VENI fellowship (016.Veni.188.040) (L.B.), by the Italian Ministry of Education, University, and Research (MIUR) – National Research Programme (PNR) – National Research Council of Italy (CNR) Flagship 'InterOmics' Project (PB.P05), by MIUR–PNR–CNR Aging program 2012–2014 (L.Z. and F.A.Z.), and by the Grigioni Foundation for Parkinson's Disease (Milan, Italy) (L.Z.).

References

- Crichton, R. (2016) *Iron Metabolism – From Molecular Mechanisms to Clinical Implications* (4th edn), Wiley
- Drayer, B. et al. (1986) MRI of brain iron. *Am. J. Roentgenol.* 147, 103–110
- Langkammer, C. et al. (2010) Quantitative MR imaging of brain iron: a postmortem validation study. *Radiology* 257, 455–462
- Stüber, C. et al. (2014) Myelin and iron concentration in the human brain: a quantitative study of MRI contrast. *NeuroImage* 93, 95–106
- Hametner, S. et al. (2018) The influence of brain iron and myelin on magnetic susceptibility and effective transverse relaxation – a biochemical and histological validation study. *NeuroImage* 179, 117–133
- Koenig, S.H. et al. (1990) Relaxometry of brain: why white matter appears bright in MRI. *Magn. Reson. Med.* 14, 482–495
- Li, W. et al. (2011) Quantitative susceptibility mapping of human brain reflects spatial variation in tissue composition. *NeuroImage* 55, 1645–1656
- Lee, J. et al. (2012) The contribution of myelin to magnetic susceptibility-weighted contrast in high-field MRI of the brain. *NeuroImage* 59, 3967–3975
- Todorich, B. et al. (2009) Oligodendrocytes and myelination: the role of iron. *Glia* 57, 467–478
- Cercignani, M. et al. (2018) *Quantitative MRI of the Brain: Principles of Physical Measurement* (2nd edn), CRC Press
- Kiselev, V.G. and Novikov, D.S. (2018) Transverse NMR relaxation in biological tissues. *NeuroImage* 182, 149–168
- Duyn, J.H. (2018) Studying brain microstructure with magnetic susceptibility contrast at high-field. *NeuroImage* 168, 152–161
- Yablonskiy, D.A. and Haacke, E.M. (1994) Theory of NMR signal behavior in magnetically inhomogeneous tissues: the static dephasing regime. *Magn. Reson. Med.* 32, 749–763
- Duyn, J.H. and Schenck, J. (2017) Contributions to magnetic susceptibility of brain tissue. *NMR Biomed.* 30, e3546
- Jochimsen, T.H. et al. (2010) Whole-brain mapping of venous vessel size in humans using the hypercapnia-induced BOLD effect. *NeuroImage* 51, 765–774
- Wehrli, F.W. et al. (2017) Susceptibility-based time-resolved whole-organ and regional tissue oximetry. *NMR Biomed.* 30, e3495
- Liu, S. et al. (2017) Susceptibility-weighted imaging: current status and future directions. *NMR Biomed.* 30, e3552
- Liu, T. et al. (2009) Calculation of susceptibility through multiple orientation sampling (COSMOS): a method for conditioning the inverse problem from measured magnetic field map to susceptibility source image in MRI. *Magn. Reson. Med.* 61, 196–204
- Shmueli, K. et al. (2009) Magnetic susceptibility mapping of brain tissue *in vivo* using MRI phase data. *Magn. Reson. Med.* 62, 1510–1522
- Schweser, F. et al. (2011) Quantitative imaging of intrinsic tissue properties using MRI signal phase: an approach to *in vivo* brain iron metabolism? *NeuroImage* 54, 2789–2807
- Schäfer, A. et al. (2009) Using magnetic field simulation to study susceptibility-related phase contrast in gradient echo MRI. *NeuroImage* 48, 126–137
- Reichenbach, J.R. (2012) The future of susceptibility contrast for assessment of anatomy and function. *NeuroImage* 62, 1311–1315
- Liu, C. et al. (2015) Susceptibility-weighted imaging and quantitative susceptibility mapping in the brain. *J. Magn. Reson. Imaging* 42, 23–41
- Haacke, E.M. et al. (2015) Quantitative susceptibility mapping: current status and future directions. *Magn. Reson. Imaging* 33, 1–25
- Deistung, A. et al. (2017) Overview of quantitative susceptibility mapping. *NMR Biomed.* 30, e3569
- Robinson, S.D. et al. (2017) An illustrated comparison of processing methods for MR phase imaging and QSM: combining array coil signals and phase unwrapping. *NMR Biomed.* 30, e3601
- Schweser, F. et al. (2017) An illustrated comparison of processing methods for phase MRI and QSM: removal of background field contributions from sources outside the region of interest. *NMR Biomed.* 30, e3601
- Shmueli, K. et al. (2011) The contribution of chemical exchange to MRI frequency shifts in brain tissue. *Magn. Reson. Med.* 65, 35–43
- Schenck, J.F. (2003) Magnetic resonance imaging of brain iron. *J. Neurol. Sci.* 207, 99–102
- Krebs, N. et al. (2014) Assessment of trace elements in human brain using inductively coupled plasma mass spectrometry. *J. Trace Elem. Med. Biol.* 28, 1–7
- Deistung, A. et al. (2013) Toward *in vivo* histology: a comparison of quantitative susceptibility mapping (QSM) with magnitude-, phase-, and R_2^* -imaging at ultra-high magnetic field strength. *NeuroImage* 65, 299–314
- Octave, J.-N. et al. (1983) Iron uptake and utilization by mammalian cells. I: cellular uptake of transferrin and iron. *Trends Biochem. Sci.* 8, 217–220
- Haacke, E.M. et al. (2005) Imaging iron stores in the brain using magnetic resonance imaging. *Magn. Reson. Imaging* 23, 1–25
- Zucca, F.A. et al. (2017) Interactions of iron, dopamine and neuromelanin pathways in brain aging and Parkinson's disease. *Prog. Neurobiol.* 155, 96–119
- Ropele, S. and Langkammer, C. (2017) Iron quantification with susceptibility. *NMR Biomed.* 30, e3534
- Lee, J. et al. (2010) On the contribution of deoxy-hemoglobin to MRI gray-white matter phase contrast at high field. *NeuroImage* 49, 193–198

37. Wharton, S. and Bowtell, R. (2012) Fiber orientation-dependent white matter contrast in gradient echo MRI. *Proc. Natl. Acad. Sci. U. S. A.* 109, 18559–18564
38. Liu, C. *et al.* (2012) 3D fiber tractography with susceptibility tensor imaging. *NeuroImage* 59, 1290–1298
39. Does, M.D. (2018) Inferring brain tissue composition and microstructure via MR relaxometry. *NeuroImage* 182, 136–148
40. Sled, J.G. (2018) Modelling and interpretation of magnetization transfer imaging in the brain. *NeuroImage* 182, 128–135
41. Stanisz, G.J. *et al.* (1999) Characterizing white matter with magnetization transfer and T_2 . *Magn. Reson. Med.* 42, 1128–1136
42. Bjarnason, T.A. *et al.* (2005) Characterization of the NMR behavior of white matter in bovine brain. *Magn. Reson. Med.* 54, 1072–1081
43. Barta, R. *et al.* (2015) Modeling T_1 and T_2 relaxation in bovine white matter. *J. Magn. Reson.* 259, 56–67
44. Whittall, K.P. and MacKay, A.L. (1989) Quantitative interpretation of NMR relaxation data. *J. Magn. Reson.* 84, 134–152
45. MacKay, A. *et al.* (1994) *In vivo* visualization of myelin water in brain by magnetic resonance. *Magn. Reson. Med.* 31, 673–677
46. Prasloski, T. *et al.* (2012) Rapid whole cerebrum myelin water imaging using a 3D GRASE sequence. *NeuroImage* 63, 533–539
47. Du, Y.P. *et al.* (2007) Fast multislice mapping of the myelin water fraction using multicompartment analysis of T_2 decay at 3T: a preliminary postmortem study. *Magn. Reson. Med.* 58, 865–870
48. Alonso-Ortiz, E. *et al.* (2018) Multi-gradient-echo myelin water fraction imaging: comparison to the multi-echo-spin-echo technique. *Magn. Reson. Med.* 79, 1439–1446
49. Laule, C. *et al.* (2008) Myelin water imaging of multiple sclerosis at 7 T: correlations with histopathology. *NeuroImage* 40, 1575–1580
50. West, K.L. *et al.* (2018) Myelin volume fraction imaging with MRI. *NeuroImage* 182, 511–521
51. Sled, J.G. *et al.* (2004) Regional variations in normal brain shown by quantitative magnetization transfer imaging. *Magn. Reson. Med.* 51, 299–303
52. Harkins, K.D. *et al.* (2012) Effect of intercompartmental water exchange on the apparent myelin water fraction in multiexponential T_2 measurements of rat spinal cord. *Magn. Reson. Med.* 67, 793–800
53. Dortch, R.D. *et al.* (2013) Characterizing inter-compartmental water exchange in myelinated tissue using relaxation exchange spectroscopy. *Magn. Reson. Med.* 70, 1450–1459
54. Labadie, C. *et al.* (2014) Myelin water mapping by spatially regularized longitudinal relaxographic imaging at high magnetic fields. *Magn. Reson. Med.* 71, 375–387
55. Henkelman, R.M. *et al.* (1993) Quantitative interpretation of magnetization transfer. *Magn. Reson. Med.* 29, 759–766
56. Gochberg, D.F. and Gore, J.C. (2003) Quantitative imaging of magnetization transfer using an inversion recovery sequence. *Magn. Reson. Med.* 49, 501–505
57. Pampel, A. *et al.* (2015) Orientation dependence of magnetization transfer parameters in human white matter. *NeuroImage* 114, 136–146
58. Schmierer, K. *et al.* (2007) Quantitative magnetization transfer imaging in postmortem multiple sclerosis brain. *J. Magn. Reson. Imaging* 26, 41–51
59. Gochberg, D.F. and Gore, J.C. (2007) Quantitative magnetization transfer imaging via selective inversion recovery with short repetition times. *Magn. Reson. Med.* 57, 437–441
60. Sled, J.G. and Pike, G.B. (2000) Quantitative interpretation of magnetization transfer in spoiled gradient echo MRI sequences. *J. Magn. Reson.* 145, 24–36
61. Müller, D.K. *et al.* (2013) Matrix-algebra-based calculations of the time evolution of the binary spin-bath model for magnetization transfer. *J. Magn. Reson.* 230, 88–97
62. Rooney, W.D. *et al.* (2007) Magnetic field and tissue dependencies of human brain longitudinal $^1\text{H}_2\text{O}$ relaxation *in vivo*. *Magn. Reson. Med.* 57, 308–318
63. Bock, N.A. *et al.* (2013) Optimizing T_1 -weighted imaging of cortical myelin content at 3.0 T. *NeuroImage* 65, 1–12
64. Oakden, W. *et al.* (2017) Early regional cuprizone-induced demyelination in a rat model revealed with MRI. *NMR Biomed.* 28, e3743
65. Lutti, A. *et al.* (2014) Using high-resolution quantitative mapping of R_1 as an index of cortical myelination. *NeuroImage* 93, 176–188
66. Weiskopf, N. *et al.* (2013) Quantitative multi-parameter mapping of R_1 , PD^* , MT , and R_2^* at 3T: a multi-center validation. *Front. Neurosci.* 7, 95
67. Metere, R. *et al.* (2017) Simultaneous quantitative MRI mapping of T_1 , T_2^* and magnetic susceptibility with multi-echo MP2RAGE. *PLoS One* 12, e0169265
68. Cercignani, M. and Bouyagoub, S. (2018) Brain microstructure by multi-modal MRI: is the whole greater than the sum of its parts? *NeuroImage* 182, 117–127
69. Weiskopf, N. *et al.* (2015) Advances in MRI-based computational neuroanatomy: from morphometry to *in-vivo* histology. *Curr. Opin. Neurol.* 28, 313–322
70. Hentze, M.W. *et al.* (2010) Two to tango: regulation of mammalian iron metabolism. *Cell* 142, 24–38
71. Kühn, L.C. (2009) How iron controls iron. *Cell Metab.* 10, 439–441
72. Muckenthaler, M.U. *et al.* (2017) A red carpet for iron metabolism. *Cell* 168, 344–361
73. Simpson, I.A. *et al.* (2015) A novel model for brain iron uptake: introducing the concept of regulation. *J. Cereb. Blood Flow Metab.* 35, 48–57
74. Burkhart, A. *et al.* (2016) Expression of iron-related proteins at the neurovascular unit supports reduction and reoxidation of iron for transport through the blood-brain barrier. *Mol. Neurobiol.* 53, 7237–7253
75. Ward, R.J. *et al.* (2014) The role of iron in brain ageing and neurodegenerative disorders. *Lancet Neurol.* 13, 1045–1060
76. Chen, P. *et al.* (2017) Effects of alpha-lipoic acid on expression of iron transport and storage proteins in BV-2 microglia cells. *Pharmacol. Rep.* 69, 1–5
77. Zhang, X. *et al.* (2006) Cellular iron status influences the functional relationship between microglia and oligodendrocytes. *Glia* 54, 795–804
78. Todorich, B. *et al.* (2011) H-ferritin is the major source of iron for oligodendrocytes. *Glia* 59, 927–935
79. Chiou, B. *et al.* (2018) Semaphorin4A and H-ferritin utilize Tim-1 on human oligodendrocytes: a novel neuro-immune axis. *Glia* 66, 1317–1330
80. Ghosh, M.C. *et al.* (2015) Iron misregulation and neurodegenerative disease in mouse models that lack iron regulatory proteins. *Neurobiol. Dis.* 81, 66–75
81. Zumbrennen-Bullough, K.B. *et al.* (2014) Abnormal brain iron metabolism in *Irf2* deficient mice is associated with mild neurological and behavioral impairments. *PLoS One* 9, e98072
82. Urrutia, P. *et al.* (2013) Inflammation alters the expression of DMT1, FPN1 and hepcidin, and it causes iron accumulation in central nervous system cells. *J. Neurochem.* 126, 541–549
83. You, L.-H. *et al.* (2017) Astrocyte hepcidin is a key factor in LPS-induced neuronal apoptosis. *Cell Death Dis.* 8, e2676
84. Connor, J.R. (2013) Iron and glia. In *Neuroglia* (3rd edn) (Kettenmann, H. and Ransom, B.R., eds), pp. 586–602, Oxford University Press
85. Hare, D.J. *et al.* (2016) Laser ablation-inductively coupled plasma-mass spectrometry imaging of white and gray matter iron distribution in Alzheimer's disease frontal cortex. *NeuroImage* 137, 124–131
86. Connor, J.R. and Menzies, S.L. (1996) Relationship of iron to oligodendrocytes and myelination. *Glia* 17, 83–93
87. Sánchez-Abarca, L.I. *et al.* (2001) Oligodendrocytes use lactate as a source of energy and as a precursor of lipids. *Glia* 36, 321–329
88. Taylor, E.M. and Morgan, E.H. (1990) Developmental changes in transferrin and iron uptake by the brain in the rat. *Dev. Brain Res.* 55, 35–42
89. Yu, G.S.M. *et al.* (1986) Effect of prenatal iron deficiency on myelination in rat pups. *Am. J. Pathol.* 125, 620–624
90. Ortiz, E. *et al.* (2004) Effect of manipulation of iron storage, transport, or availability on myelin composition and brain iron

- content in three different animal models. *J. Neurosci. Res.* 77, 681–689
91. Lozoff, B. *et al.* (2006) Long-lasting neural and behavioral effects of iron deficiency in infancy. *Nutr. Rev.* 64, S34–S43 Discussion S72–S91
 92. Oloyede, O.B. *et al.* (1992) Effects of low-iron status and deficiency of essential fatty acids on some biochemical constituents of rat brain. *Biochem. Int.* 27, 913–922
 93. Duncan, G.W. *et al.* (2016) Gray and white matter imaging: a biomarker for cognitive impairment in early Parkinson's disease? *Mov. Disord.* 31, 103–110
 94. Bouhrara, M. *et al.* (2018) Evidence of demyelination in mild cognitive impairment and dementia using a direct and specific magnetic resonance imaging measure of myelin content. *Alzheimers Dement.* 14, 998–1004
 95. Ali-Rahmani, F. *et al.* (2014) H63D mutation in hemochromatosis alters cholesterol metabolism and induces memory impairment. *Neurobiol. Aging* 35, 1511.e1–1511.e12
 96. Dusek, P. and Schneider, S.A. (2012) Neurodegeneration with brain iron accumulation. *Curr. Opin. Neurol.* 25, 499–506
 97. Meadowcroft, M.D. *et al.* (2016) Reduced white matter MRI transverse relaxation rate in cognitively normal H63D-HFE human carriers and H67D-HFE mice. *Brain Imaging Behav.* 10, 1231–1242
 98. Saher, G. and Stumpf, S.K. (2015) Cholesterol in myelin biogenesis and hypomyelinating disorders. *Biochim. Biophys. Acta* 1851, 1083–1094
 99. Zywickie, H.A. *et al.* (2002) Microscopic R2* mapping of reduced brain iron in the Belgrade rat. *Ann. Neurol.* 52, 102–105
 100. Grishchuk, Y. *et al.* (2015) Impaired myelination and reduced brain ferric iron in the mouse model of mucopolidosis IV. *Dis. Model. Mech.* 8, 1591–1601
 101. Zecca, L. *et al.* (2004) The role of iron and copper molecules in the neuronal vulnerability of locus coeruleus and substantia nigra during aging. *Proc. Natl. Acad. Sci. U. S. A.* 101, 9843–9848
 102. Ramos, P. *et al.* (2014) Iron levels in the human brain: a post-mortem study of anatomical region differences and age-related changes. *J. Trace Elem. Med. Biol.* 28, 13–17
 103. Sedlak, J. *et al.* (2014) Reversible, irreversible and effective transverse relaxation rates in normal aging brain at 3 T. *NeuroImage* 84, 1032–1041
 104. Connor, J.R. *et al.* (1995) A quantitative analysis of isoferitins in select regions of aged, Parkinsonian, and Alzheimer's diseased brains. *J. Neurochem.* 65, 717–724
 105. Zecca, L. *et al.* (2008) New melanic pigments in the human brain that accumulate in aging and block environmental toxic metals. *Proc. Natl. Acad. Sci. U. S. A.* 105, 17567–17572
 106. Zecca, L. *et al.* (2004) Iron, brain ageing and neurodegenerative disorders. *Nat. Rev. Neurosci.* 5, 863–873
 107. Connor, J.R. *et al.* (1992) A histochemical study of iron, transferrin and ferritin in Alzheimer's diseased brains. *J. Neurosci. Res.* 31, 75–83
 108. Smith, M.A. *et al.* (1997) Iron accumulation in Alzheimer disease is a source of redox-generated free radicals. *Proc. Natl. Acad. Sci. U. S. A.* 94, 9866–9868
 109. Everett, J. *et al.* (2014) Evidence of redox-active iron formation following aggregation of ferrihydrite and the Alzheimer's disease peptide β -amyloid. *Inorg. Chem.* 53, 2803–2809
 110. Collingwood, J.F. and Telling, N.D. (2016) Iron oxides in the human brain. In *Iron Oxides: From Nature to Applications* (Faivre, D., ed.), pp. 143–176, Wiley-VCH
 111. Bulk, M. *et al.* (2018) Quantitative comparison of different iron forms in the temporal cortex of Alzheimer patients and control subjects. *Sci. Rep.* 8, 6898
 112. House, M.J. *et al.* (2008) 1.4T study of proton magnetic relaxation rates, iron concentrations, and plaque burden in Alzheimer's disease and control postmortem brain tissue. *Magn. Reson. Med.* 60, 41–52
 113. Ayton, S. *et al.* (2017) Cerebral quantitative susceptibility mapping predicts amyloid- β -related cognitive decline. *Brain* 140, 2112–2119
 114. Tao, Y. *et al.* (2014) Perturbed iron distribution in Alzheimer's disease serum, cerebrospinal fluid, and selected brain regions: a systematic review and meta-analysis. *J. Alzheimers Dis.* 42, 679–690
 115. Kirschvink, J.L. *et al.* (1992) Magnetite biomineralization in the human brain. *Proc. Natl. Acad. Sci. U. S. A.* 89, 7683–7687
 116. Gossuin, Y. *et al.* (2005) Looking for biogenic magnetite in brain ferritin using NMR relaxometry. *NMR Biomed.* 18, 469–472
 117. Maher, B.A. *et al.* (2016) Magnetite pollution nanoparticles in the human brain. *Proc. Natl. Acad. Sci. U. S. A.* 113, 10797–10801
 118. Gilder, S.A. *et al.* (2018) Distribution of magnetic remanence carriers in the human brain. *Sci. Rep.* 8, 11363
 119. Lopes, K.O. *et al.* (2008) Microglial dystrophy in the aged and Alzheimer's disease brain is associated with ferritin immunoreactivity. *Glia* 56, 1048–1060
 120. Theofilas, P. *et al.* (2017) Locus coeruleus volume and cell population changes during Alzheimer's disease progression: a stereological study in human postmortem brains with potential implication for early-stage biomarker discovery. *Alzheimers Dement.* 13, 236–246
 121. Liu, K.Y. *et al.* (2017) Magnetic resonance imaging of the human locus coeruleus: a systematic review. *Neurosci. Biobehav. Rev.* 83, 325–355
 122. Dexter, D.T. *et al.* (1991) Alterations in the levels of iron, ferritin and other trace metals in Parkinson's disease and other neurodegenerative diseases affecting the basal ganglia. *Brain* 114, 1953–1975
 123. Faucheux, B.A. *et al.* (2003) Neuromelanin associated redox-active iron is increased in the substantia nigra of patients with Parkinson's disease. *J. Neurochem.* 86, 1142–1148
 124. Yu, X. *et al.* (2013) Decreased iron levels in the temporal cortex in postmortem human brains with Parkinson disease. *Neurology* 80, 492–495
 125. Zhang, W. *et al.* (2011) Neuromelanin activates microglia and induces degeneration of dopaminergic neurons: implications for progression of Parkinson's disease. *Neurotox. Res.* 19, 63–72
 126. Schwarz, S.T. *et al.* (2017) *In vivo* assessment of brainstem depigmentation in Parkinson disease: potential as a severity marker for multicenter studies. *Radiology* 283, 789–798
 127. Sulzer, D. *et al.* (2018) Neuromelanin detection by magnetic resonance imaging (MRI) and its promise as a biomarker for Parkinson's disease. *NPJ Park. Dis.* 4, 11
 128. Prasad, S. *et al.* (2018) Three-dimensional neuromelanin-sensitive magnetic resonance imaging of the substantia nigra in Parkinson's disease. *Eur. J. Neurol.* 25, 680–686
 129. Fabbri, M. *et al.* (2017) Substantia nigra neuromelanin as an imaging biomarker of disease in Parkinson's disease. *J. Park. Dis.* 7, 491–501
 130. Martin-Bastida, A. *et al.* (2017) Brain iron chelation by deferiprone in a phase 2 randomised double-blinded placebo controlled clinical trial in Parkinson's disease. *Sci. Rep.* 7, 1398
 131. Trujillo, P. *et al.* (2017) Contrast mechanisms associated with neuromelanin-MRI. *Magn. Reson. Med.* 78, 1790–1800
 132. Vavasour, I.M. *et al.* (2018) Global loss of myelin water over 5 years in multiple sclerosis normal-appearing white matter. *Mult. Scler. J.* 24, 1557–1568
 133. O'Muircheartaigh, J. *et al.* (2019) Quantitative neuroimaging measures of myelin in the healthy brain and in multiple sclerosis. *Hum. Brain Mapp.* 40, 2104–2116
 134. Bagnato, F. *et al.* (2011) Tracking iron in multiple sclerosis: a combined imaging and histopathological study at 7 Tesla. *Brain* 134, 3602–3615
 135. Wisniewski, C. *et al.* (2015) Quantitative susceptibility mapping (QSM) of white matter multiple sclerosis lesions: interpreting positive susceptibility and the presence of iron. *Magn. Reson. Med.* 74, 564–570
 136. Langkammer, C. *et al.* (2018) Quantitative susceptibility mapping: report from the 2016 reconstruction challenge. *Magn. Reson. Med.* 89, 1161–1673
 137. Hawrylycz, M.J. *et al.* (2012) An anatomically comprehensive atlas of the adult human brain transcriptome. *Nature* 489, 391–399
 138. Patrick, P.S. *et al.* (2016) Development of Tm2d as a reporter gene for MRI. *Magn. Reson. Med.* 75, 1697–1707

139. Massner, C. *et al.* (2018) Genetically controlled lysosomal entrapment of superparamagnetic ferritin for multimodal and multiscale imaging and actuation with low tissue attenuation. *Adv. Funct. Mater.* 28, 1706793
140. Kumar, P. *et al.* (2016) A novel approach to quantify different iron forms in *ex-vivo* human brain tissue. *Sci. Rep.* 6, 38916
141. Meyers, S.M. *et al.* (2017) Simultaneous measurement of total water content and myelin water fraction in brain at 3 T using a T_2 relaxation based method. *Magn. Reson. Imaging* 37, 187–194
142. Birk, C. *et al.* (2016) Effects of formalin fixation and temperature on MR relaxation times in the human brain. *NMR Biomed.* 29, 458–465
143. Zecca, L. *et al.* (1994) Iron and other metals in neuromelanin, substantia nigra, and putamen of human brain. *J. Neurochem.* 62, 1097–1101
144. Connor, J.R. (1994) Isoforms of ferritin have a specific cellular distribution in the brain. *J. Neurosci. Res.* 37, 461–465
145. Quintana, C. and Gutiérrez, L. (2010) Could a dysfunction of ferritin be a determinant factor in the aetiology of some neurodegenerative diseases? *Biochim. Biophys. Acta* 1800, 770–782
146. Zucca, F.A. *et al.* (2018) Neuromelanin organelles are specialized autolysosomes that accumulate undegraded proteins and lipids in aging human brain and are likely involved in Parkinson's disease. *NPJ Park. Dis.* 4, 17
147. Papaefthymiou, G.C. (2009) Nanoparticle magnetism. *Nano Today* 4, 438–447
148. Makhlof, S.A. *et al.* (1997) Magnetic hysteresis anomalies in ferritin. *Phys. Rev. B* 55, R14717–R14720
149. Gossuin, Y. *et al.* (2009) Magnetic resonance relaxation properties of superparamagnetic particles. *WIREs Nanomed. Nanobiotechnol.* 1, 299–310
150. Nakane, T. *et al.* (2008) Visualization of neuromelanin in the substantia nigra and locus ceruleus at 1.5T using a 3D-gradient echo sequence with magnetization transfer contrast. *Magn. Reson. Med. Sci.* 7, 205–210
151. Goya, G.F. *et al.* (2003) Static and dynamic magnetic properties of spherical magnetite nanoparticles. *J. Appl. Phys.* 94, 3520–3528
152. Dhital, B. *et al.* (2016) Temperature dependence of water diffusion pools in brain white matter. *NeuroImage* 127, 135–143
153. Tardif, C.L. *et al.* (2015) Multi-contrast multi-scale surface registration for improved alignment of cortical areas. *NeuroImage* 111, 107–122
154. Nieuwenhuys, R. and Broere, C.A.J. (2017) A map of the human neocortex showing the estimated overall myelin content of the individual architectonic areas based on the studies of Adolf Hopf. *Brain Struct. Funct.* 222, 465–480
155. Sherman, D.L. and Brophy, P.J. (2005) Mechanisms of axon ensheathment and myelin growth. *Nat. Rev. Neurosci.* 6, 683–690
156. Min, Y. *et al.* (2009) Interaction forces and adhesion of supported myelin lipid bilayers modulated by myelin basic protein. *Proc. Natl. Acad. Sci. U. S. A.* 106, 3154–3159